

1 Technical Note: Rapid multi-exponential curve fitting algorithm for voxel-based targeted radionuclide
2 dosimetry

3 Key words: Radionuclide dosimetry, pharmacokinetics, image processing

4

5 Price Jackson^{1,2}

6 Lachlan McIntosh¹

7 Michael S. Hofman^{1,2}

8 Grace Kong^{1,2}

9 Rodney J. Hicks^{1,2}

10

11 ¹Department of Molecular Imaging & Therapeutic Nuclear Medicine, Peter MacCallum Cancer Centre,
12 Melbourne, Australia 3000

13 ²Sir Peter MacCallum Department of Oncology, University of Melbourne, Melbourne, Australia 3010

14 Corresponding Author: Price Jackson

15 Email: price.jackson@petermac.org

16 Address: Dept of Physical Sciences, 305 Grattan St, Melbourne VIC, 3000, Australia

17

18 Short Title: Tri-exponential kinetics Algorithm

19 Abstract:

20 Background: Dosimetry in nuclear medicine often relies on estimating pharmacokinetics based on
21 sparse temporal data. As analysis methods move toward image-based 3-dimensional computation, it
22 becomes important to interpolate and extrapolate these data without requiring manual intervention; that
23 is, in a manner that is highly efficient and reproducible. Iterative least-squares solvers are poorly suited
24 to this task because of the computational overhead and potential to optimise to local minima without
25 applying tight constraints at the outset.

26 Methodology: This work describes a fully-analytical method for solving three-phase exponential time-
27 activity curves based on three measured time points in a manner that may be readily employed by

This is the author manuscript accepted for publication and has undergone full peer review but has not been through the copyediting, typesetting, pagination and proofreading process, which may lead to differences between this version and the [Version of Record](#). Please cite this article as [doi: 10.1002/MP.14243](https://doi.org/10.1002/MP.14243)

This article is protected by copyright. All rights reserved

28 image-based dosimetry tools. The methodology uses a series of conditional statements and a piecewise
29 approach for solving exponential slope directly through measured values in most instances. The
30 proposed algorithm is tested against a purpose-designed iterative fitting technique and linear piecewise
31 method followed by single exponential in a cohort of 10 patients receiving ^{177}Lu -DOTA-Octreotate
32 therapy.

33 Results: Tri-exponential time-integrated values are shown to be comparable to previously-published
34 methods with an average difference between organs when computed at the voxel level of $9.8\pm 14.2\%$
35 and $-3.6\pm 10.4\%$ compared to iterative and interpolated methods, respectively. Of the three methods,
36 the proposed tri-exponential algorithm was most consistent when regional time-integrated activity was
37 evaluated at both voxel- and whole-organ levels. For whole-body SPECT imaging, it is possible to
38 compute 3D time-integrated activity maps in less than 5 minutes processing time. Further, the technique
39 is able to predictably and reproducibly handle artefactual measurements due to noise or spatial
40 misalignment over multiple image times.

41 Conclusions: An efficient, analytical algorithm for solving multi-phase exponential pharmacokinetics is
42 reported. The method may be readily incorporated into voxel-dose routines by combining with widely
43 available image registration and radiation transport tools.

44

45 Keywords: radionuclide dosimetry, pharmacokinetics, image processing

46

47

48 Main Text:

49 Background:

50 Driven by increasing recognition of the clinical benefits of radionuclide therapy, particularly in
51 neuroendocrine tumors and prostate cancer^{1,2}, image-based dosimetry in nuclear medicine has been a
52 focus of physics and computational development. The MIRD committee has published coefficients for
53 estimating radiation transport from sources at the voxel level³ and other groups have supplemented
54 these tables for a variety of cubic dimensions and common therapeutic isotopes^{4,5}. This has been
55 extended to patient-specific Monte Carlo calculations, which may now be performed in a clinically-
56 achievable timeframe^{6,7}. There has been consideration of the spatial effects of ionisation relative to
57 source location with respect to the resolution of the imaging systems used to infer that source
58 distribution⁸. There has also been work extending dose metrics to infer radiobiological effect according
59 to dose-rate and spatial heterogeneity⁹.

60 While much focus has been applied to computation of radiation physics, research in pharmacokinetic
61 interpolation is relatively limited. Inferring the input time-integrated activity map—a 3-dimensional grid

62 of the number of disintegrations per voxel—represents a comparably challenging task both in terms of
63 complexity and potential to introduce errors in the predicted dose-volume. In the ideal instance, this is
64 performed entirely in the image space allowing dosimetry to be appreciated at the level of detail attained
65 by a SPECT imaging system. Typically, this workflow involves serial acquisition of multiple quantitative
66 SPECT images¹⁰ with pharmacokinetic time-activity curves (TACs) derived independently for each
67 position in the aligned image sequence¹¹.

68 One of the primary challenges in computing voxelized TACs is employing a routine that is
69 generalizable—that is, one that can be applied uniformly throughout the variety of tissues in the body—
70 while operating without manual oversight and at minimal concession to fitting accuracy. Sarrut *et al.*
71 described an algorithm that places voxels into different classes to simplify the optimisation challenge
72 and penalise models based on their complexity¹². This, in principle, yields more reproducible results
73 than an unconstrained least-squares method. A similar approach had previously been employed by
74 Kletting *et al.* to enable users to designate between a variety of fitting functions based on the shape of
75 pharmacokinetic measurements, however, in requiring user input would not be appropriate for voxel
76 level dose estimation¹³. In this work a general three-phase exponential model is applied which offers
77 the flexibility to characterise components of uptake as well as a mixture of slow and fast tissue clearance
78 components.

79 An analytical pharmacokinetic estimation technique is reported in detail including the sequence of
80 computational operations and methods for handling noisy or otherwise irregular data. The technique
81 provides the basis for a previously-published voxel dosimetry software package¹⁴ and has been shown
82 to be reliable across a variety of clinical trial datasets¹⁵. Given that all phases of the pharmacokinetic
83 curves—even those of uptake—may be described by equations of exponential decay, it is possible to
84 approach the problem as a piecewise operation. By solving for the slope between the final two
85 measurements, the preceding phases can be solved in sequence moving to earlier times based on the
86 difference between measured values and the trajectory of the previously predicted phase as a simplified
87 curve-stripping process¹⁶. Depending on the data conditions, where measurement values lie within
88 respective reference lines, the most appropriate order of solving may vary. In some instances, for
89 example when activity continues to increase beyond the second image time, the curve is best
90 approximated by only two phases using sustained uptake from injection to the final measurement,
91 followed by physical decay in the period beyond. This facilitates simplification of a highly unconstrained
92 problem—six variables with only three data points—using only a few straightforward assumptions and
93 computational logic operations. With judicious selection of acquisition times, this form of curve
94 generation may be applied in a manner that is representative, and without systematic bias, for a wide
95 variety of pharmacokinetic models.

96 Methods:

97 With the aim to solve parameters that define a three-phase exponential curve described by Equation 1,
98 A_{1-3}/k_{1-3} , the ideal case includes a single phase of tissue uptake and up to two phases of clearance.

99 This model may describe periods of rapid washout and long-term retention; each with a variable half-
100 life and relative proportion as represented across a variety of pharmacokinetic tissue types.

101
$$\text{Region Activity} = A_1e^{k_1t} + A_2e^{k_2t} + A_3e^{k_3t}$$

102 **Equation 1**

103 [Figure 1]

104 Three activity concentration values are described as c_{1-3} and time points as t_{1-3} . As a preliminary step,
105 the convention is taken to decay-correct all image data, $c_{i1-3} \rightarrow c_{1-3}$, as illustrated in Figure 1. This
106 handles concentration values in pharmacological terms during fitting. The decay-correction is
107 straightforward to reverse when taking the final integral calculation and offers practical advantage to
108 ensure that the pharmacological concentration does not continue to increase beyond the final imaging
109 time point. This should be a reasonable assumption given judicious selection of imaging time points¹⁷.
110 Specifically, it prevents the final integral from exceeding a value that would exceed the physical half-life
111 of the isotope; curves which deplete more slowly than the half-life of the radionuclide. If the highest
112 activity measurement is detected at the final time point, fitting a slope very near zero, $k_3 \approx -\infty$, equates to
113 only physical decay. Secondly, this provides a simple mechanism to adapt the algorithm for other
114 isotope or diagnostic/therapeutic pairs, for example using sequential ¹²⁴I PET/CT imaging to predict
115 radiation dose from ¹³¹I radioactive iodine. The user only needs to provide the physical half-life of each
116 tracer and the same algorithm may be applied to compute local time-integrated activity concentration
117 (decays per unit volume) for the given quantity of activity administered.

118 [Figure 2]

119 The ideal case can be described by a transient uptake phase between $t=0$ and t_1 followed by distinct
120 periods of rapid and delayed washout in the $t_{1 \rightarrow 2}$ and $t_{2 \rightarrow 3}$ time spans, respectively, as shown in Figure
121 2. In clinical use of long half-life therapeutic isotopes, after initial uptake, one or two exponential
122 clearance phases of activity from organs and tumors are widely described¹⁸. It is possible to fit a curve
123 of exponential decay between two points as shown in Figure 3 with the form:

124
$$A = A_0e^{kt}$$

125 **Equation 2**

126 Solving for the linear fit, $y = mx + b$, by log transform of the activity values starting with the final phase,
127 the kinetic parameter, k_3 , is determined by:

128
$$k_3 = m = \frac{\ln(c_3) - \ln(c_2)}{t_3 - t_2}$$

129 **Equation 3:**

130 And the amplitude parameter, A_3 , is then:

131

$$A_3 = e^b = e^{\ln(c_2) - k_3 t_2}$$

132 **Equation 4:**

133 [Figure 3]

134 As a first instance, this method provides the slope of the line representing the long-term retention phase.
 135 The preceding phase can be described as the difference between the slope described by the A_3, k_3
 136 curve and the value at c_1 using another exponential decay equation that depletes as it approaches t_2 .
 137 This very nearly builds a piecewise function from exponential terms. Solving by log transform requires
 138 non-zero values, so, for simplicity, we adjust the latter activity value, delta c_2 , to be in the range of 1-
 139 3% of the measured value c_2 . Some discussion of the special conditions which warrant the variability is
 140 provided in later sections. The process may be more clearly illustrated by the mixture of curves in Figure
 141 4. The residual of the curve, Δc_1 , is the difference between the slope of the late phase and the first
 142 measured activity value, c_1 :

143

$$\Delta c_1 = c_1 - A_3 e^{k_3 t_1}$$

144 **Equation 5:**

145 The sign of the delta value is evaluated: $\Delta c_2 = 0.01 * c_2$ if Δc_1 is greater than zero. If not, the sign is
 146 reversed to $\Delta c_2 = -0.01 * c_2$. That is, both delta values should be positive or negative. There are
 147 conditions when a negative A_2 provides the most appropriate fit based on the measured data. Curve
 148 approximation then follows the previous method of solving for exponential slope to generate a phase
 149 that depletes as it approaches c_2 :

150

$$k_2 = \frac{\ln(\Delta c_2) - \ln(\Delta c_1)}{t_2 - t_1}$$

151

$$A_2 = e^{\ln(\Delta c_1) - k_2 t_1}$$

152 **Equation 6:**

153 [Figure 4]

154 Estimating the very early uptake kinetics requires an approximation when there are no intermediate
 155 points before the peak activity measurement. This is typical when only one image is available during
 156 the first day of administration. One approach is to infer the uptake pharmacokinetics based on a generic
 157 rate constant, k_1 . For long half-life therapeutic isotopes, the majority of the time-integrated activity
 158 calculation is dictated by the late-phase retention. That is, if the physical half-life is several days or
 159 longer, only select tissues with significant initial uptake followed by rapid and sustained clearance could
 160 be appreciably impacted by the use of a generic uptake parameter. The notable exception is choosing
 161 a very small k_1 parameter representing very rapid uptake. In this case, the presented algorithm may
 162 yield a curve that escalates dramatically at times close to $t=0$ due to the nature of solving the line-of-fit
 163 for the fast clearance phase. With ^{177}Lu , a half-time of approximately 30 minutes, $k_1 = -1.3$, has been

164 shown to offer reasonable agreement with other curve-fitting integrals over a range of different tissue
165 types^{14,19}. An analysis of the influence of the generic rate parameter on time-integrated activity is
166 provided in Supplementary Table 1 showing that over a range of half-times from 20 to 90 minutes, the
167 effect is in the order of $\pm 2\%$ except in bladder and heart (blood pool). Finally, the amplitude, A_1 , of the
168 uptake phase is set such that concentration value passes through zero at $t=0$. Here the term A_1
169 becomes the negative of the sum of A_2 and A_3 .

170 In this manner, it is possible to analytically solve a three-phase exponential that very closely passes
171 through three measured time points. This piecewise method, or a slightly modified version, can be
172 applied wherever declining slope is detected between values of c_2 and c_3 ; that is, whenever some
173 clearance is detected in the late phase of imaging as would be typical of most tracers and tissue types.
174 The sequence of computations is depicted in the flowchart shown by Supplementary Figure 6 with this
175 common case designated by bold labels.

176 With the solved time-activity curve, it is then possible to integrate the decay-corrected curve from $t_0 \rightarrow \infty$
177 including the physical half-life of the isotope in the form:

$$\tilde{A} = \frac{A_1}{\left(\frac{\ln 2}{t_{1/2}} + k_1\right)} + \frac{A_2}{\left(\frac{\ln 2}{t_{1/2}} + k_2\right)} + \frac{A_3}{\left(\frac{\ln 2}{t_{1/2}} + k_3\right)}$$

179 **Equation 7:**

180 Where \tilde{A} is the time-integrated activity or total number of disintegrations in the region described by the
181 time-activity curve, $t_{1/2}$ is the physical half-life of the therapeutic isotope, and the parameters A_{1-3} and
182 k_{1-3} are the fitting values described previously.

183 A detailed explanation of conditional methods to derive curves for irregular, or slowly-accumulating data
184 is provided in the supplementary material (Supplementary Figures 1-3). This involves methods to
185 classify the shape of the curve to apply algorithmic steps suited to that pharmacokinetic type. In some
186 instances, such as when activity decreases from c_1 to c_2 and increases again at c_3 the algorithm will
187 interpolate an intermediate location to analytically define a curve that balances the necessary error
188 between measurements with a behaviour that is similar to least-squares optimisation. It is worth noting
189 that for these cases, the convention is taken to define a curve that as often as possible passes directly
190 through the final measurement time—typically the most important for long half-life isotopes—and
191 subsequently mitigate the error for the line-of-fit that passes through or near the preceding times. Flow
192 charts to illustrate the conditional sequence of processing are given in Supplementary Figures 4-6.

193 The multi-exponential algorithm was tested in clinical application in a representative cohort of 10
194 patients receiving ¹⁷⁷Lu-DOTA-Octreotate. Cases were followed-up by serial post-treatment quantitative
195 SPECT imaging at timelines of 4, 24, & 72 hours. Pharmacokinetics were then computed at the voxel
196 level with the proposed tri-exponential algorithm. For comparison to two reference methodologies, time-
197 integrated activity was estimated by piecewise linear approximation between image times followed by
198 a single exponential phase determined by the effective half-life over the final two image acquisitions²⁰.

199 In voxels where the detected clearance rate was slower than the physical half-life of ^{177}Lu , clearance
200 was instead based on physical decay. Secondly, the iterative fitting technique described by Sarrut *et*
201 *al.*, the Voxel-based Multimodal method (VoMM), was implemented with Python libraries^{12,21}. In that
202 method, iterative optimization is performed for each voxel according to four different single- or multi-
203 exponential models and the most accurate line-of-fit with a penalty for model complexity is chosen. The
204 resulting time-integrated activity concentration for each technique was compared both at the voxel level
205 and based on a single curve derived from the mean activity in each volume-of-interest. For tumor and
206 a selection of relevant tissues (kidney, spleen, liver, bladder, marrow, etc) time-integrated activity was
207 assessed. Additionally the mean absolute error as weighted for voxel activity in predicted curves with
208 the tri-exponential algorithm and VoMM method was investigated for each imaging time point. The
209 median of all cases with each technique is summarized.

210 Results:

211 This work presents a computationally efficient methodology to solve highly unconstrained curve fitting
212 in a predictable manner. The authors have previously demonstrated that this algorithm yields
213 comparable regional dosimetry when applied independently across regional voxels to whole-organ
214 methods employed with OLINDA coupled with a traditional iterative curve solver^{14,19}. In comparison to
215 alternative voxel methods including trapezoidal interpolation followed by a single exponential and the
216 previously published VoMM iterative technique, closest agreement between methods was observed in
217 long-retaining tissues. Time-integrated activity in high-uptake organs (kidney, liver, spleen)—those
218 considered at-risk in ^{177}Lu -Ocreotat therapy—was on average within 10% for all curve fitting methods
219 evaluated at the voxel level. Results for the 10 patient cohort are summarised in Table 1 and an
220 evaluation of median voxel-wise fitting error at each of the three imaging time points is reported for the
221 tri-exponential and VoMM techniques in Table 2. The three methods were observed to be in closer
222 agreement when pharmacokinetics were computed at the organ- rather than voxel-level where the tri-
223 exponential algorithm was within 5% of the VoMM technique for all regions except for bladder, intestines
224 and pancreas. Of the three, the proposed tri-exponential algorithm most closely reproduces the whole
225 organ time integrated activity result when calculated from independent voxel curves with the lowest
226 variation observed for 8 of the 15 regions including tumor, marrow, liver, and left kidney.

227 In comparison to a trapezoidal interpolation followed by single-exponential model, the multi-exponential
228 model was typically 3.5% lower in terms of estimated integral decays with most organs in the range of
229 -1 to -8%. Much of the area under the curve for these therapies is dictated by the late phase retention
230 which should be similar in most cases with single- and tri-exponential evaluations. A significant
231 difference in dose to bladder is reported with all three methods which may be attributed to the relative
232 variation in uptake between images on the first day of therapy and those acquired at 24 hours and
233 beyond. Where tissues displaying this form of clearance are relevant for assessing potential toxicity, it
234 is advisable to collect finer temporal sampling in the first day post-administration.

235 The scripted implementation of the fitting algorithm using Python computes at a rate of approximately
236 5,000 voxels per second with clinical image data^{14,22}. Applying a condition to ignore background

237 voxels—those with very low activity values—dose volumes for a multi-bed SPECT series at 3.0mm
238 cubic spatial resolution can be computed in less than five minutes. Processing times were comparable
239 to trapezoidal and single-exponential model. The iterative VoMM method was considerably more
240 computationally intensive, previously reported at 800 voxels per second¹², however the python-based
241 implementation would not be practical to apply across the full image space and voxel-wise fitting was
242 restricted to labelled subregions. Image-based pharmacokinetics processing is often coupled with non-
243 rigid image registration to tightly fuse the serial time points across the image volume²³. That step will
244 typically be equally or more computationally intensive than the pharmacokinetics process described in
245 this work and as such this method of pharmacokinetic interpolation should not be considered a
246 significant bottleneck to clinical workflows. As a complete image-based dosimetry tool, the algorithm
247 has been employed in a variety of clinical studies for both therapeutic and diagnostic dose evaluation
248 which have been used to inform patient management²⁴⁻²⁷.

249 [Table 1]

250 The overall residual error was observed to be comparable between iteratively optimized and tri-
251 exponential algorithms, however, the VoMM method was shown to be most accurate at the early image
252 phase with increasing error at later time points. This is to be anticipated as the observed activity—and
253 potential to influence sum of squared error—carries less weight for the optimization task. In contrast,
254 the proposed tri-exponential algorithm is designed to fit directly through the 2nd and 3rd measurements
255 wherever the shape of the curve would sensibly permit. This may necessarily come at the sacrifice of
256 accuracy in the very early phases; for example, in bowel which can be slow to accumulate ¹⁷⁷Lu-
257 Octreotate over several days.

258 [Table 2]

259 Discussion:

260 This work aims to describe an automated, reproducible and efficient methodology for solving a large
261 volume of time-activity curves with application to nuclear medicine dosimetry. The choice of three-phase
262 exponential model affords the flexibility to characterise periods of tracer uptake as well as mixtures of
263 slow- and fast-clearance. By considering the sequence of operations, it is possible to address model
264 over-complexity: solving the most important phase at the outset and applying additional phases as
265 necessary with decreasing influence on the time integral. The resulting algorithm is designed to yield
266 comparable estimates of time-integrated activity to traditional methods including linear piecewise
267 interpolation or constrained least-squares optimisation. Additionally as a pure exponential model, it is
268 straightforward to apply isotope decay corrections and integral calculations. Many of the standard
269 kinetic coefficients selected in the present implementation are chosen empirically as a practical solution
270 for use in ¹⁷⁷Lu-DOTA-octreotate dosimetry and with imaging times routinely used in clinical practice.
271 The conditional methods have been shown to reliably approximate time-integrated activity estimates
272 from other curve-fitting techniques when compared both at the voxel and organ level.

273 It has been consistently reported that delayed image acquisitions are most important to accurately
274 estimate dosimetry in ^{177}Lu therapies even for complex pharmacokinetic models^{28,29}. The algorithm in
275 this work is designed to yield curves which pass through the final acquisition time and, where
276 appropriate, will directly determine late phase clearance based on the line of slope between the second
277 and third image acquisitions. This is in contrast to most iterative least-squares solvers which, in the
278 ordinary case, will be weighted toward uptake when activity is largest, typically at the earliest time point
279 and may be at the expense of accurately characterizing time-integrated activity. This can be improved
280 upon by modifying the objective function to bias the weighting of certain measurements either explicitly
281 or through additional iterative operations³⁰, but this presents a different set of challenges if the aim is
282 to implement as a general purpose tool to efficiently run in the image space. Balancing patient
283 convenience with quantitative accuracy and ease of use is a motivation for improved algorithms for
284 clinical dosimetry.

285 There are intrinsic limitations to fitting a six-variable equation to three measured data points; or
286 effectively four if directed through zero at the origin and generic uptake rates are considered. Even with
287 well-conditioned data, the combination of clearance half-times and fractions may be modified to yield
288 an infinite number of solutions which pass through the measurement values. This is constrained if each
289 phase of the multi-exponential term depletes to very near zero as it transitions from one measurement
290 to the next. Subsequently, the shape of the curve is influenced by the selection of image times as the
291 inflection between phases 2 and 3 will necessarily occur at the second measurement time. If the time
292 points are not chosen sensibly, or there are inconsistencies in the image times between patients within
293 a cohort, systematic bias could result. This, however, is a challenge for any pharmacokinetic
294 assessment methodology and it is worthwhile to restate the importance of judicious selection of
295 measurements with consideration of the pharmacokinetics and physical half-life of any
296 radiopharmaceutical. Of specific note, when using short half-life isotopes or imaging in the first two
297 hours of administration, it is advisable to experiment with the standard uptake rate coefficient, k_1 , which
298 may be modified (and likely reduced) to reliably model the underlying physiology. As with the selection
299 of uptake half-time, the use of conditional assumptions may warrant special consideration for the
300 pharmacokinetics of individual tracers with ^{124}I , ^{131}I and ^{90}Y being of particular interest in the context of
301 current therapeutic radionuclides. Additionally, with increasing focus on the potential for theranostic
302 isotope pairs such as $^{86}\text{Y}/^{90}\text{Y}$, $^{44}\text{Sc}/^{47}\text{Sc}$, or $^{64}\text{Cu}/^{67}\text{Cu}$ which permit delayed, high-resolution imaging
303 and treatment with an equivalent molecular species, the ability to assess pharmacokinetics in the image
304 space is particularly relevant.

305 In this report, a working version of the algorithm is distributed as open-source software, which may be
306 employed directly or improved upon by contributing researchers. Because the algorithm runs with a set
307 of conditional statements and a sequence for solving for exponential slope between two points, it is
308 possible to implement in software that handles basic conditional and mathematical operations. For
309 demonstration or use as a region-based dosimetry tool, the algorithm has been incorporated into an
310 interactive spreadsheet, which is available in the supplementary material supporting this article or at
311 the primary author's Github repository³¹.

312 Conclusions:

313 This report presents a generalizable algorithm to derive time-activity curves from limited temporal
314 measurement data. The methodology relies on separating the curve-fitting challenge into piecewise
315 phases similarly to a residual stripping technique. Conditional statements allow the process to be
316 applied in a predictable manner that achieves a sensible compromise in error for voxels which may be
317 subject to noise or inconsistent co-registration. The technique is computationally efficient allowing use
318 for routine image-based dosimetry. A complete version of the algorithm is provided as open-source
319 computer code for developers of nuclear medicine analysis software.

320

321 Acknowledgements:

322 PJ is supported by a Victorian Cancer Agency clinical fellowship. Initial clinical data provided through
323 grant support by the Victorian Cancer Agency clinical trial, “GaTate-PET/CT to predict LuTate dosimetry
324 in patients with neuroendocrine tumour disease: a pilot study” (CI RJH). MSH is supported by a Clinical
325 Fellowship Award from the Peter MacCallum Foundation and receives grants from the Prostate Cancer
326 Foundation (PCF), Movember, U.S. Department of Defence and the Prostate Cancer Foundation of
327 Australia. He also receives research funding from Advanced Accelerator Applications (a Novartis
328 company). GK is supported by a Clinical Fellowship Award from the Peter MacCallum Foundation. RJH
329 is recipient of a National Health and Medical Research Council Practitioner Fellowship (APP1108050).
330 The authors would like to thank David Sarrut for his advice and input in evaluating the methodology in
331 comparison to his previously published technique.

332

333 Conflicts-of-interest:

334 The authors have no conflicts to disclose

335

336 Citations:

- 337 1. Fanti S, Minozzi S, Antoch G, et al. Consensus on molecular imaging and theranostics in
338 prostate cancer. *The Lancet Oncology*. 2018;19(12):e696-e708.
- 339 2. Kwekkeboom DJ, Krenning EP, Lebtahi R, et al. ENETS consensus guidelines for the standards
340 of care in neuroendocrine tumors: peptide receptor radionuclide therapy with radiolabeled
341 somatostatin analogs. *Neuroendocrinology*. 2009;90(2):220-226.
- 342 3. Bolch WE, Bouchet LG, Robertson JS, et al. MIRD pamphlet no. 17: the dosimetry of
343 nonuniform activity distributions—radionuclide S values at the voxel level. *Journal of Nuclear
344 Medicine*. 1999;40(1):11S-36S.

- 345 4. Lanconelli N, Pacilio M, Meo SL, et al. A free database of radionuclide voxel S values for the
346 dosimetry of nonuniform activity distributions. *Physics in Medicine & Biology*. 2012;57(2):517.
- 347 5. Dieudonné A, Hobbs RF, Bolch WE, Sgouros G, Gardin I. Fine-resolution voxel S values for
348 constructing absorbed dose distributions at variable voxel size. *Journal of nuclear medicine*.
349 2010;51(10):1600-1607.
- 350 6. Pacilio M, Lanconelli N, Lo Meo S, et al. Differences among Monte Carlo codes in the
351 calculations of voxel values for radionuclide targeted therapy and analysis of their impact on
352 absorbed dose evaluations. *Medical physics*. 2009;36(5):1543-1552.
- 353 7. Jackson PA, Hickson K. Integration of GATE Monte Carlo-based radionuclide dosimetry as a
354 practical on-line clinical tool. Paper presented at: 2017 Geant4 User Workshop2017;
355 University of Wollongong, Wollongong, Australia.
- 356 8. Pacilio M, Amato E, Lanconelli N, et al. Differences in 3D dose distributions due to calculation
357 method of voxel S-values and the influence of image blurring in SPECT. *Physics in Medicine &*
358 *Biology*. 2015;60(5):1945.
- 359 9. Sgouros G, Frey E, Wahl R, He B, Prideaux A, Hobbs R. Three-dimensional imaging-based
360 radiobiological dosimetry. Paper presented at: Seminars in nuclear medicine2008.
- 361 10. Dewaraja YK, Frey EC, Sgouros G, et al. MIRD pamphlet no. 23: quantitative SPECT for patient-
362 specific 3-dimensional dosimetry in internal radionuclide therapy. *Journal of Nuclear*
363 *Medicine*. 2012;53(8):1310-1325.
- 364 11. Ljungberg M, Celler A, Konijnenberg MW, Eckerman KF, Dewaraja YK, Sjögren-Gleisner K.
365 MIRD pamphlet no. 26: joint EANM/MIRD guidelines for quantitative ¹⁷⁷Lu SPECT applied for
366 dosimetry of radiopharmaceutical therapy. *Journal of nuclear medicine*. 2016;57(1):151-162.
- 367 12. Sarrut D, Halty A, Badel JN, Ferrer L, Bardiès M. Voxel-based multimodel fitting method for
368 modeling time activity curves in SPECT images. *Medical physics*. 2017;44(12):6280-6288.
- 369 13. Kletting P, Schimmel S, Kestler H, et al. Molecular radiotherapy: The NUKFIT software for
370 calculating the time-integrated activity coefficient. *Medical physics*. 2013;40(10):102504.
- 371 14. Jackson PA, Beauregard JM, Hofman MS, Kron T, Hogg A, Hicks RJ. An automated voxelized
372 dosimetry tool for radionuclide therapy based on serial quantitative SPECT/CT imaging.
373 *Medical physics*. 2013;40(11).
- 374 15. Violet J, Jackson P, Ferdinandus J, et al. Dosimetry of ¹⁷⁷Lu-PSMA-617 in Metastatic
375 Castration-Resistant Prostate Cancer: Correlations Between Pretherapeutic Imaging and
376 Whole-Body Tumor Dosimetry with Treatment Outcomes. *Journal of Nuclear Medicine*.
377 2019;60(4):517-523.

- 378 16. Kirkup L, Sutherland J. Curve stripping and nonlinear fitting of polyexponential functions to
379 data using a microcomputer. *Computers in Physics*. 1988;2(6):64-68.
- 380 17. Siegel JA, Thomas SR, Stubbs JB, et al. MIRD pamphlet no. 16: techniques for quantitative
381 radiopharmaceutical biodistribution data acquisition and analysis for use in human radiation
382 dose estimates. *Journal of Nuclear Medicine*. 1999;40(2):37S-61S.
- 383 18. Stabin M, Xu XG. Basic principles in the radiation dosimetry of nuclear medicine. Paper
384 presented at: Seminars in nuclear medicine 2014.
- 385 19. Stabin MG, Sparks RB, Crowe E. OLINDA/EXM: the second-generation personal computer
386 software for internal dose assessment in nuclear medicine. *Journal of nuclear medicine*.
387 2005;46(6):1023-1027.
- 388 20. Grassi E, Fioroni F, Ferri V, et al. Quantitative comparison between the commercial software
389 STRATOS[®] by Philips and a homemade software for voxel-dosimetry in radiopeptide therapy.
390 *Physica Medica*. 2015;31(1):72-79.
- 391 21. Virtanen P, Gommers R, Oliphant TE, et al. SciPy 1.0: fundamental algorithms for scientific
392 computing in Python. *Nature Methods*. 2020:1-12.
- 393 22. Van Der Walt S, Colbert SC, Varoquaux G. The NumPy array: a structure for efficient numerical
394 computation. *Computing in Science & Engineering*. 2011;13(2):22.
- 395 23. Klein S, Staring M, Murphy K, Viergever MA, Pluim JP. Elastix: a toolbox for intensity-based
396 medical image registration. *IEEE transactions on medical imaging*. 2010;29(1):196-205.
- 397 24. Willowson KP, Ryu H, Jackson P, Singh A, Eslick E, Bailey DL. A comparison of 2D and 3D kidney
398 absorbed dose measures in patients receiving ¹⁷⁷Lu-DOTATATE. *Asia Oceania Journal of*
399 *Nuclear Medicine and Biology*. 2018;6(2):113.
- 400 25. Hicks RJ, Jackson P, Kong G, et al. First-in-human trial of ⁶⁴Cu-SARTATE PET imaging of patients
401 with neuroendocrine tumours demonstrates high tumor uptake and retention, potentially
402 allowing prospective dosimetry for peptide receptor radionuclide therapy. *Journal of Nuclear*
403 *Medicine*. 2018:jnumed. 118.217745.
- 404 26. Pattison DA, Solomon B, Hicks RJ. A new theranostic paradigm for advanced thyroid cancer.
405 *Journal of Nuclear Medicine*. 2016;57(10):1493-1494.
- 406 27. Kong G, Callahan J, Hofman MS, et al. High clinical and morphologic response using ⁹⁰Y-DOTA-
407 octreotate sequenced with ¹⁷⁷Lu-DOTA-octreotate induction peptide receptor
408 chemoradionuclide therapy (PRCRT) for bulky neuroendocrine tumours. *European journal of*
409 *nuclear medicine and molecular imaging*. 2017;44(3):476-489.

- 410 28. Hänscheid H, Lapa C, Buck AK, Lassmann M, Werner RA. Absorbed dose estimates from a
411 single measurement one to three days after the administration of ^{177}Lu -DOTATATE/-TOC.
412 *Nuklearmedizin*. 2017;56(06):219-224.
- 413 29. Madsen MT, Menda Y, O'Dorisio TM, O'Dorisio MS. Single time point dose estimate for
414 exponential clearance. *Medical physics*. 2018;45(5):2318-2324.
- 415 30. Muzic Jr RF, Christian BT. Evaluation of objective functions for estimation of kinetic
416 parameters. *Medical physics*. 2006;33(2):342-353.
- 417 31. Jackson PA. Github - TriExponential-Solver. 2019;
418 <https://github.com/jacksonmedphysics/TriExponential-Solver>.

419

420

421 Supplementary Material:

422 Handling of irregular data:

423 When performing operations across many thousands of voxels that may be prone to noise or image
424 alignment errors, there are likely to be challenging locations that warrant special consideration to yield
425 curves and integrals which represent fair approximations of the underlying data. In instances where the
426 highest activity is detected at t_3 , a reasonable convention is to assume that only physical decay occurs
427 at time points beyond²⁰; or for simplicity that there is very slight pharmacological clearance such that
428 the effective half-time is determined by the physical half-life of the isotope as illustrated in
429 Supplementary Figure 1. In the proposed method, setting k_3 to a value near zero yields an equivalent
430 computation when applied to decay-corrected data. The coefficient A_3 may be solved according to
431 Equation 4. There may be no need to fit multiple uptake phases in this instance ($A_2=0$). Instead, the
432 method from Equation 6 is used to solve for a single uptake phase that reaches a maximum as it nears
433 c_3 . There is scope to moderate the uptake kinetics based on the measured data points c_1 and c_2 , as
434 illustrated in the flow chart shown by Supplementary Figure 5. Nevertheless, the area under the curve
435 for long half-life isotopes will be primarily dictated by the amplitude of uptake at measurement c_3 . In
436 other instances, this type of curve may be physiologically appropriate.

437 [Supplementary Figure 1]

438 The most apparent case where the data requires correction from the outset is when the trajectory of
439 uptake or clearance changes multiple times across the measurement points. This may occur when a
440 region initially displays a large activity concentration that appears to decrease at the time of the second
441 image and subsequently increases again at the third. In image-based dosimetry, these instances are
442 often artefactual; produced due to noise or small misalignments near the margin of high-uptake tissues
443 such as kidneys and spleen. Here, the aim is to mitigate potential errors and yield a curve that
444 approximates the behaviour of a least-squares fitting routine. In this methodology, the convention is

445 taken that the final time point is most important to determine the time integral. The values of the first
446 two points are moderated such that it is possible to apply a curve solving methodology which balances
447 error with respect to the early phase(s) as shown in Supplementary Figure 2.

448 [Supplementary Figure 2]

449 Solving exponential slope between values that transition to very near zero can be problematic. This
450 tends to occur for voxels in low-uptake regions where small changes in absolute activity concentration
451 represents very large relative differences if one of the values is near zero. Although this type of
452 measurement is largely influenced by scanner sensitivity in background regions and reconstructed
453 noise, using those rate kinetics parameters leaves the potential to infer extremely high uptake in the
454 very early time window and, as such, overestimate time-integrated activity. As a practical fix, the relative
455 uptake can be initially compared across time-points and adjusted if necessary—in this case c_3 is
456 modified to 10% of the value at c_2 as shown in the preconditioning flow-chart, Supplementary Figure
457 4—to yield a more sensible curve and estimate of integral decays.

458 Additionally, computation of two threshold c_2 values are used to define the limits for the slope between
459 the values of c_1 and c_3 . The first, $c_{2,plateau}$, is used to test whether activity increases between time points
460 2 and 3. If the activity at c_1 is also very low, as may occur in some tissues that slowly accumulate tracer
461 such as bowel in ^{177}Lu -PMSA therapy, no correction would be warranted. In other cases where activity
462 initially declines from c_1 to c_2 only to increase again at the final measurement such as shown in
463 Supplementary Figure 2, it is logical to assume that some element of the measurement is artefactual.
464 Shifting the value of c_2 up to the plateau point where the exponential fit between c_2 and c_3 achieves
465 minimal biological clearance; or effectively only physical decay from t_2 and passing through the
466 measurement c_3 . With this parameter solved, it is then possible to apply the piecewise methodology to
467 solve the remaining phases that may appropriately to pass through c_1 .

468 [Supplementary Figure 3]

469 When the concentration at c_2 appears as less than a linear interpolation between time points c_1 and c_3
470 (illustrated in Supplementary Figure 3), a solution is to compute a value that falls on that line, $c_{2,linear}$,
471 that may replace the original value if increasing slope is required to approximate the curve up to the
472 final imaging time. The resulting curve is illustrated in Supplementary Figure 3 and the implementation
473 into the algorithmic workflow can be traced in Supplementary Figure 5 and Supplementary Figure 6.

474 [Supplementary Figure 4]

475 [Supplementary Figure 5]

476 [Supplementary Figure 6]

477

478 Selection of Generic Uptake Rate Parameter (k_1):

479 For the common condition where fast- and slow-clearance components are observed it is sensible to
480 implement a generic uptake rate in order to prevent unrealistically large activity extrapolations in the
481 times between $t=0$ and the first measurement. By setting the amplitude parameter A_1 equal to the
482 negative sum of the A_2 and A_3 coefficients, the curve will necessarily pass through the origin at the
483 time of administration and a generic k_1 coefficient should be applied which allows uptake to complete
484 prior to the measurement (typically in the first several hours) but mitigates the potential for large
485 area under the curve in the initial moments post-administration. In this instance, an empirically chosen
486 k_1 value of -1.3 (approximately 30 minutes half-time) appears to provide a reasonable approximation
487 for a variety of tissue types. The results of experiments with other rate parameters for half-times of
488 20, 60, and 90 minutes are provided in Supplementary Table 1 and yield time-integrated activity values
489 within 2% in all instances, except in tissues with a particularly large component of early-phase
490 clearance such as urinary bladder and heart (blood pool).

491 [Supplementary Table 1]

492

493 Figure Captions:

494 Figure 1: Decay-correcting initial measured data before fitting ensures algorithm does not fit
495 increasing pharmacological concentration beyond final imaging time point. This is accounted for when
496 calculating time-integrated activity and easily permits estimates from diagnostic/therapeutic isotope
497 pairs such as $^{124}\text{I}/^{131}\text{I}$.

498 Figure 2 - Illustration of typical time-activity curve comprised of three exponential phases that has
499 been solved to pass through measured data points. Plots of the component exponential curves, one
500 uptake and two clearance, are shown as dashed lines. The sum of phases 2 & 3 and all phases are
501 shown as shown as solid green and solid blue, respectively. Note that phase 1 and phase 2 effectively
502 deplete as the curve nears measurement time points 1 & 2.

503 Figure 3 - Standard (left) and logarithmic (right) plots of method to solve late-phase clearance based
504 on exponential slope between measurement time points 2 and 3.

505 Figure 4 - Method to solve phase 2, first clearance phase, based on the difference in the curve
506 described by Figure 2 and the measured activity at time point 1. Standard (left) and logarithmic (right)
507 plots are shown to illustrate piecewise nature of the individual curve phases.

508 Supplementary Figure 1: Time-activity curve approximated for data with greatest uptake measured at
509 the final time point c_3 . Physical decay is assumed beyond and a single uptake phase may be used to

510 approximate the kinetics between $t=0$ and c_3 . Dotted line represents the late-phase retention beyond
511 c_3 . On right plot, separate phases are plotted individually; uptake phase shown as dashed line. The
512 resulting time-activity curve is shown as solid line against measured values on left.

513 Supplementary Figure 2: Example of serial activity measurements requiring conditional adjustment to
514 solve analytical time-activity curve. This may occur due to image alignment issues or noise and is
515 unlikely to represent true physiology. Here the activity declines at c_2 and increases again at c_3 . This
516 may be detected by conditional statement and the measurement c_2 is adjusted to match the slope for
517 very near physical clearance between time-points c_2 and c_3 . The piecewise solving process may then
518 proceed as normal.

519 Supplementary Figure 3: A second pattern of measurement that may be detected by conditional
520 statement. By first shifting the measured activity at c_2 to the linear interpolation between c_1 and c_3 ,
521 solving with the piecewise algorithm approximates the behaviour of a least-squares optimiser, yielding
522 a curve that is a compromise of early measured data.

523 Supplementary Figure 4: Initial preconditioning of values with very low measurements relative to the
524 second time point. These tend to occur in low-uptake regions or where there are errors in image
525 alignment and this may prevent calculation of very large exponential decay slopes.

526 Supplementary Figure 5: Calculation of comparison values $c_{2, \text{plateau}}$ and $c_{2, \text{linear}}$ which may be employed
527 to handle unrealistic cases (eg. high-low-high uptake).

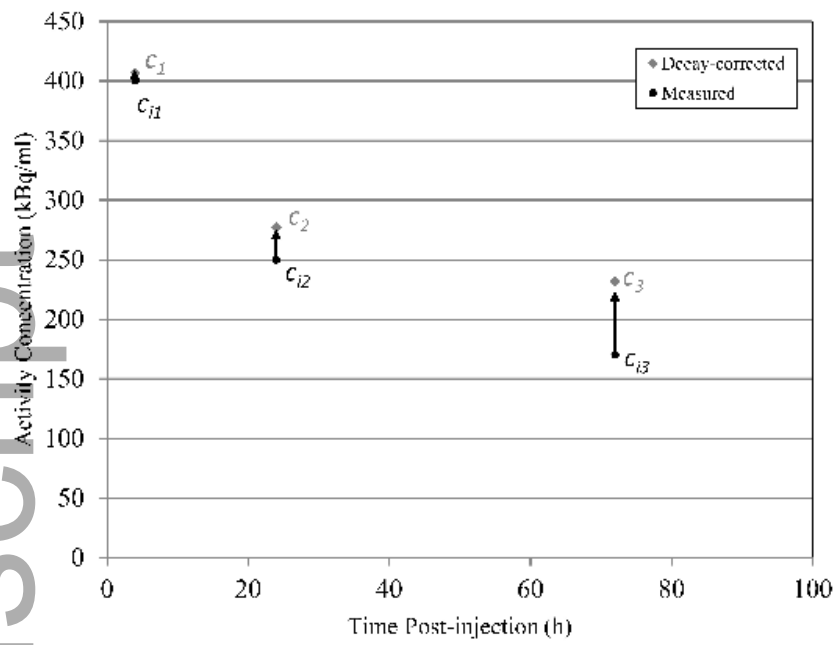
528 Supplementary Figure 6 - Primary flow-chart for solving time-activity curve as a two- or three-phase
529 exponential decay curve. Note: the common case with one uptake phase and two separate clearance
530 components is denoted in bold.

Table 1 - Estimated time-integrated activity for representative cohort of ¹⁷⁷Lu-DOTA-Octreotate therapies as computed using proposed tri-exponential algorithm, Voxel-based Multimodal, and simplified piecewise with single late-phase exponential methods. Results are provided based on curves computed at the voxel level (mean of all curves) and additionally based on a single curve for each organ using the mean activity concentration at each timepoint.

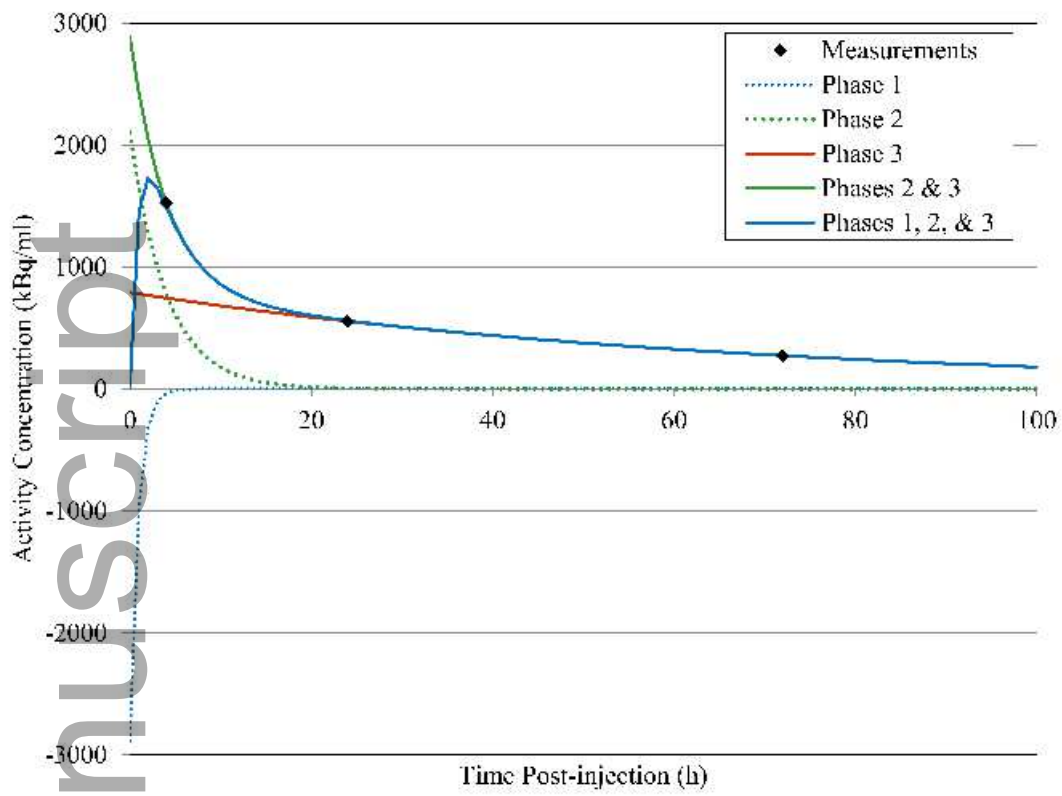
	Mean Time-Integrated Activity Concentration (MBq*h/ml)					
	Voxel Level:	Whole Organ:				
	<u>Tri-exponential</u>	<u>VoMM</u>	<u>Trapezoid + Single Exponential</u>	<u>Tri-exponential</u>	<u>VoMM</u>	<u>Trapezoid + Single Exponential</u>
Marrow	2.78	2.52	2.95	2.78	2.86	2.88
Muscle	1.21	1.22	1.28	1.03	1.06	1.05
Lung	1.01	1.04	1.11	0.95	0.96	1.04
Heart	1.62	1.71	1.76	1.54	1.62	1.64
Stomach	14.92	13.86	15.57	14.03	13.51	14.39
Small Bowel	3.51	3.32	3.65	2.93	2.97	2.93
Liver	27.46	24.96	27.98	26.53	26.74	26.08
Pancreas	17.53	15.04	18.64	18.02	16.20	19.18
Spleen	56.26	52.05	57.64	53.43	53.82	52.54
Right Kidney	39.27	35.96	40.16	36.97	37.51	36.86
Left Kidney	35.88	32.61	36.38	33.99	34.88	33.98
Bladder	20.23	25.33	34.65	18.99	24.81	33.13
Lower Large Intestine	10.92	7.40	10.85	10.41	7.79	10.28
Upper Large Intestine	5.35	4.96	5.14	4.83	4.22	4.55
Tumor	327.83	290.79	345.99	330.26	347.25	351.85

Table 2 - Median Voxel Level error as relative percentage at each of the three imaging time points. Note that the iterative solving method (VoMM) is biased toward reducing error at early images as when activity and associated calculation of residual error would be greatest. The proposed tri-exponential algorithm prioritizes accuracy for the second and third measurements with consideration of the late phase influence on the estimated time integral.

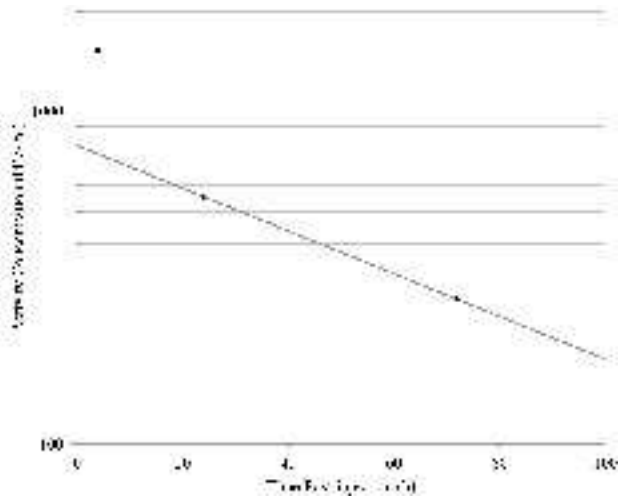
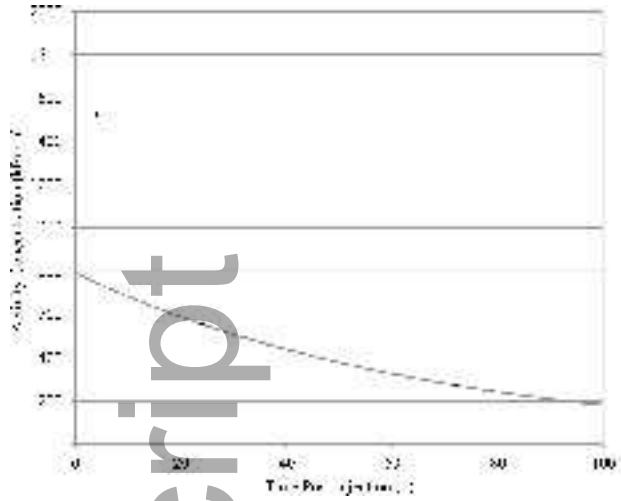
Region	4h		24h		72h	
	<u>Tri-</u> exponential	VoMM	<u>Tri-</u> exponential	VoMM	<u>Tri-</u> exponential	VoMM
Marrow	5.0%	1.4%	10.3%	7.4%	0.0%	12.2%
Muscle	3.8%	0.5%	8.2%	3.9%	0.0%	11.7%
Lung	8.4%	0.1%	5.7%	1.2%	0.0%	9.3%
Heart	5.5%	0.1%	4.9%	1.1%	0.0%	9.2%
Stomach	8.5%	4.7%	6.3%	7.2%	0.2%	7.1%
Small Bowel	12.5%	1.9%	7.6%	7.5%	0.2%	14.8%
Liver	3.2%	0.4%	1.9%	1.4%	0.1%	2.5%
Pancreas	5.7%	4.5%	12.1%	7.2%	0.1%	7.9%
Spleen	4.2%	1.1%	2.8%	3.4%	0.1%	6.2%
Right Kidney	4.3%	0.5%	1.3%	2.3%	0.1%	13.8%
Left Kidney	4.2%	0.6%	1.6%	2.7%	0.0%	14.6%
Bladder	7.2%	0.0%	1.9%	0.6%	0.0%	51.2%
Lower Large Intestine	77.0%	13.7%	3.6%	13.4%	0.1%	10.0%
Upper Large Intestine	21.4%	5.9%	2.2%	8.0%	0.2%	16.7%
Tumor	15.9%	4.7%	8.5%	7.3%	0.3%	15.2%



mp_14243_f1.jpg

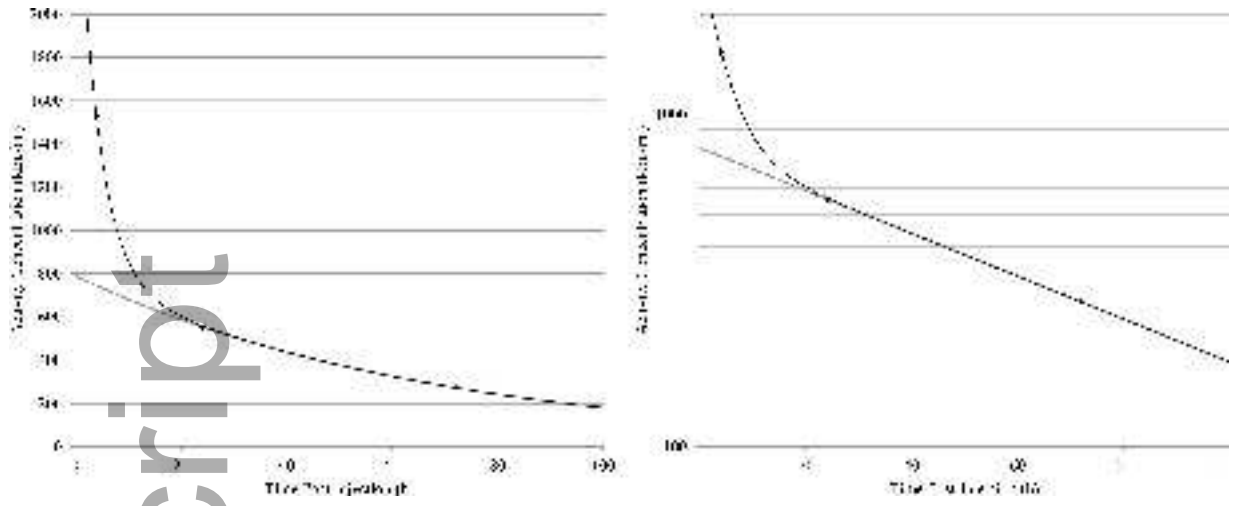


mp_14243_f2.jpg



mp_14243_f3.jpg

Author Manuscript



mp_14243_f4.jpg

Author Manuscript



Minerva Access is the Institutional Repository of The University of Melbourne

Author/s:

Jackson, P;McIntosh, L;Hofman, MS;Kong, G;Hicks, RJ

Title:

Technical Note: Rapid multiexponential curve fitting algorithm for voxel-based targeted radionuclide dosimetry

Date:

2020-06-12

Citation:

Jackson, P., McIntosh, L., Hofman, M. S., Kong, G. & Hicks, R. J. (2020). Technical Note: Rapid multiexponential curve fitting algorithm for voxel-based targeted radionuclide dosimetry. *MEDICAL PHYSICS*, 47 (9), pp.4332-4339. <https://doi.org/10.1002/mp.14243>.

Persistent Link:

<http://hdl.handle.net/11343/275895>